Effect of Body Bias on Near-Field Electron Behavior in a Magnetically Shielded Hall Thruster

Naia I. Butler-Craig,[1] Julian Lopez-Uricoechea,[1] Richeek Dutta,[1] and Mitchell L. R. Walker[1]
High-Power Electric Propulsion Laboratory, Georgia Institute of Technology, Atlanta, GA 30332, USA

(*Electronic mail: nbutlercraig3@gatech.edu)

(Dated: 4 August 2026)

This work investigates the influence of thruster body bias on near-field electron behavior in a magnetically shielded Hall effect thruster (HET) through spatially resolved laser Thomson scattering (LTS) diagnostics. Experiments were conducted on the 9-kW class H9 magnetically shielded HET operating at 40 A discharge current and 150 V discharge voltage on krypton propellant in the Georgia Tech Vacuum Test Facility 2. Three electrical configurations were examined: floating (body electrically isolated), cathode-tied (body at cathode potential, approximately -10.3 V relative to facility ground), and $+2$ V bias (body biased $+2$ V relative to ground). Spatially resolved measurements of electron density, electron temperature, and radial electron bulk velocity were obtained at up to 23 locations (a 15-point radial grid and up to eight axial stations along the cathode centerline) spanning the cathode near-field from the cathode centerline to the discharge channel centerline. A configuration-dependent spatial density inversion reveals distinct circuit topologies: at $z/r_0 = 0.029$, cathode-tied elevates n_e at the cathode centerline (4.4×10^{19} m^{-3}) while exhibiting the lowest channel-centerline density (6.6×10^{17} m^{-3}), whereas the $+2$ V configuration shows the opposite pattern (3.4×10^{19} m^{-3} and 9.0×10^{17} m^{-3}, respectively). The $+2$ V configuration exhibits the lowest T_e at the inner front pole cover, consistent with magnetization-limited, energy-selective electron collection. Electron pressure does not serve as a reliable proxy for electrostatic potential in this near-field region due to unmeasured anomalous transport terms.

I. INTRODUCTION

Hall effect thrusters (HETs) are used extensively for deep-space missions, orbital transfers, and station-keeping because of their high specific impulse and operational robustness[1]. Enhancing thruster operational lifetime remains a central challenge, particularly for magnetically shielded configurations designed to achieve extended lifetimes exceeding 10,000 hours of operation. Magnetic shielding of HET acceleration channels mitigates ion-induced erosion of channel walls by confining the intense ion bombardment to a thin magnetic field boundary layer. This technology has significantly extended thruster lifetime predictions from thousands to tens of thousands of hours[2–4]. However, erosion of the inner front pole cover (IFPC) has emerged as a potential life-limiting mechanism in magnetically shielded thrusters[5,6].

Three physical mechanisms for IFPC erosion have been hypothesized. First, radial electrostatic fields driven by electron pressure gradients in the near-field region establish electric potential variations that could drive ion trajectories toward IFPC surfaces[7]. Second, bombardment of ions originating from charge-exchange collisions in the near-field plume[8]. Third, direct impingement of high-energy ions from the acceleration channel onto the pole face surfaces[9]. This work builds upon the first mechanism, namely how electrostatic potential pathways are established through electron pressure gradients and external electrical boundary conditions. The selection of the cathode-tied configuration as the baseline flight design for magnetically shielded thrusters, established by Peterson *et al.*[10] through performance mapping of NASA's HERMeS TDU-1 across multiple electrical configurations and partially motivated by its observed mitigation of IFPC erosion, motivates the characterization of how body bias affects the near-field plasma.

The radial distribution of electrons in the cathode near-field is relevant to IFPC erosion because radial electron flux and pressure contribute to the electrostatic potential that ions experience. Spatial asymmetries in electron behavior may also serve as signatures of distinct current collection pathways at different body bias levels. IFPC erosion on the NGHT-1X thruster after extended operation has been documented photographically by Nikrant and Switzer (Fig. 9 of Ref. 9). The radial striations in that erosion pattern, reported as continuing from the channel edge onto the front-facing pole cover surface, motivate the focus of this work on radial gradients in near-field electron properties, as the erosion morphology suggests radially structured processes at the IFPC surface. Nikrant and Switzer hypothesize two distinct eroding ion populations: beam-origin ions with high radial velocities, to which they attribute the striations, and low-energy ions created and anomalously heated within the IFPC region, which erode the smooth, background-pressure-sensitive portion of the pole face[9]. The trajectories of this latter population are governed by the local electrostatic potential structure, established in part by electron pressure gradients; the radial pressure gradient from the channel centerline to the inner pole reported by Suazo Betancourt *et al.*[7] therefore motivates characterizing how the near-field electron properties, and the potentials they establish, respond to the thruster body electrical boundary condition.

However, current literature on HET near-field diagnostics has primarily focused on floating or cathode-tied body configurations, and the relative impact of different electrical boundary conditions on electron behavior has not been systematically characterized with spatially resolved, non-invasive diagnostics. This work addresses that gap using laser Thomson scattering (LTS) to obtain absolute, spatially resolved measurements of electron density (n_e), electron temperature (T_e), and radial electron bulk velocity across three body bias configurations in the near-field of a magnetically shielded HET. Spatially resolved n_e and T_e map how the electron population redistributes under different electrical boundary conditions, and differences in their spatial structure across configurations serve as indicators of distinct current closure pathways imposed by each body bias. Electron pressure and radial bulk velocity are also evaluated as potential diagnostics for local electrostatic potential structure and cross-field transport, respectively.

II. LASER THOMSON SCATTERING DIAGNOSTIC

A. Scattering Theory

Laser Thomson scattering exploits elastic scattering of laser photons by free electrons and provides direct, spatially resolved measurements of electron density and temperature without perturbing the plasma[11,12]. The technique has been applied to Hall thruster near-field plasmas by Vincent *et al.*[13,14], Tsikata *et al.*[15], and Suazo Betancourt *et al.*[7,16], who demonstrated that LTS can resolve electron properties in regions where Langmuir probes are unreliable due to their perturbative nature and the high-energy particle environment[17]. When a high-intensity laser beam passes through a plasma, electrons scatter photons with a wavelength shift due to the Doppler effect from the electrons' thermal motion. The scattered power as a function of wavelength for species i is given by

$$P_{\lambda,i}(\lambda) = P_0 n_i f \frac{d\sigma_i}{d\Omega} L \Delta\Omega S_{\lambda,i}(\lambda), \tag{1}$$

where P_0 is the incident laser power, n_i is the electron density, f is the solid angle collection factor, $d\sigma_i/d\Omega$ is the differential scattering cross section, L is the scattering volume length, $\Delta\Omega$ is the collection solid angle, and $S_{\lambda,i}(\lambda)$ is the spectral density function. The spectral density function for electrons is a Gaussian for a Maxwellian velocity distribution:

$$S_{\lambda,e}(\lambda) = \frac{1}{\sqrt{\pi}\Delta\lambda_D} \exp\left[-\left(\frac{\lambda-\lambda_0}{\Delta\lambda_D}\right)^2\right], \tag{2}$$

where $\Delta\lambda_D$ is the Doppler width, related to electron temperature by

$$\Delta\lambda_D = \frac{\lambda_0}{c}\sqrt{\frac{8 k_B T_e \ln 2}{m_e}}. \tag{3}$$

The electron density is obtained from the integrated area of the scattered spectrum, which is proportional to n_e through the known Thomson scattering cross section and the calibration factor determined from rotational Raman scattering in air. The electron temperature is obtained from the Gaussian width of the scattered spectrum through Eq. (3). When a net electron bulk velocity is present, the centroid of the scattered spectrum shifts from λ_0 by an amount proportional to the bulk velocity component along the scattering wave vector, enabling measurement of directed electron motion.

The scattering parameter α determines the character of the scattering[11,12]. For this work, $\alpha \ll 1$ throughout the measurement domain, establishing the incoherent scattering regime[13,15]. In this regime, scattering occurs from individual electrons rather than collective plasma oscillations, and the measured spectral profile directly yields n_e, T_e, and bulk velocity without plasma dispersion models. For the cathode-tied and $+2$ V configurations, data processing uses a theoretical Gaussian instrument function convolved with the modeled Thomson spectrum and fit to the raw spectral data using nonlinear least-squares optimization, yielding fitted parameters for electron density, electron temperature, and bulk velocity.

B. Signal Isolation and Data Processing

Isolating the Thomson signal from competing emission sources requires a multi-spectrum acquisition strategy [7,13,14]. Four spectra are collected at each measurement location: (A) laser-on with thruster operating, (B) laser-off with thruster operating (emission), (C) laser-on with thruster off (reflection), and (D) laser-off with thruster off (background). The Thomson signal is then isolated as

$$S_{\text{Thomson}} = A - (B + C - D). \tag{4}$$

This four-spectrum approach effectively subtracts stray light, thruster self-emission, laser reflection on chamber surfaces, and electronic background. Residual stray light near the laser line wavelength λ_0, originating primarily from elastic scattering of the laser beam off chamber walls and optical surfaces, is removed by an automatic exclusion factor algorithm that masks spectral pixels within a wavelength window of λ_0 (typically $\sim$1 nm) during the fitting procedure. For the floating configuration, spectral asymmetry was observed; the origin of this distortion was not determined, but it was resolved analytically by incorporating the measured spectrograph instrument function (obtained by imaging a narrow-linewidth spectral lamp) as an asymmetric response in the fitting model.

C. Uncertainty Quantification

Model parameters were optimized using the Levenberg–Marquardt algorithm[18] to minimize the residual between the measured Thomson spectrum and the forward-convolved model. Parameter uncertainties are quantified from the nonlinear least-squares covariance matrix[11]. For a fit with parameters $\boldsymbol{p}$ and residual sum of squares SSR, the covariance matrix is

$$\text{Cov}(\boldsymbol{p}) = \frac{\text{SSR}}{N-M}\left(\boldsymbol{J}^T\boldsymbol{J}\right)^{-1}, \tag{5}$$

where N is the number of spectral points, M is the number of fitted parameters, and $\boldsymbol{J}$ is the Jacobian matrix. The diagonal elements of $\mathrm{Cov}(\boldsymbol{p})$ provide variance estimates, and the square roots yield parameter uncertainties. Electron density uncertainty is further propagated from the fitted amplitude and temperature using the off-diagonal covariance terms to account for parameter correlation[7,13].

Typical uncertainties achieved in this work are approximately 0.5% for electron density and 0.1% for electron temperature, reflecting the high signal-to-noise ratio at the 40 A, 150 V operating condition. These values represent measurement precision and do not account for systematic uncertainties in spectral calibration or spatial location determination, which are estimated at the few-percent level.

III. EXPERIMENTAL SETUP

A. Vacuum Test Facility and Thruster

Experiments were conducted using the H9 magnetically shielded HET[4] in the Vacuum Test Facility 2 (VTF-2) at the Georgia Tech High-Power Electric Propulsion Laboratory (HPEPL). VTF-2 is a 9.2 m long, 4.9 m diameter stainless steel chamber evacuated by ten liquid-nitrogen-cooled CVI TMI reentrant cryopumps. The H9 is a 9-kW class thruster designed for geostationary satellite station-keeping and primary propulsion for small spacecraft. Figure 1 shows the LTS diagnostic installed in VTF-2 with the H9.

Research-grade krypton (99.999% purity) was supplied to the anode and cathode through two MKS GE50A mass flow controllers, each calibrated against a MesaLabs DryCal 800-10 volumetric flow meter. Anode and cathode flow rates were 402 ± 4.0 sccm-Kr and 28 ± 0.31 sccm-Kr, respectively, yielding a facility background pressure of 7.73 μTorr-Kr (corrected for krypton). The discharge was driven by an EMI/TDK-Lambda EMHP 600 Vdc, 100 Adc power supply with a 95-μF capacitor and 1.3-Ω resistor LC filter. Auxiliary power supplies included TDK-Lambda GEN60-25 (cathode heater), GEN40-38 (inner magnet), and GEN80-42 (outer magnet).

The thruster was operated at a nominal discharge current of 40 A and 150 V. The magnetic field was set to 87.5% of the nominal field configuration specified in design documentation, as established by Su *et al.*[19]. Detailed magnetic field topology, field magnitudes, and absolute dimensions of the H9 are export controlled and are therefore reported only in normalized form throughout this work: the field as a percentage of the nominal setting, and the geometry normalized by the channel centerline radius r_0 (Figs. 4–6), consistent with prior H9 publications[4,19]. The thruster was operated for 3 hours prior to data collection to allow thermal and operational stabilization. These conditions were held constant across all three electrical configurations; the only independent variable was the thruster body electrical boundary condition. Operating conditions and telemetry are summarized in Table I. Operational stability was verified by telemetry monitoring, and discharge current fluctuations and breathing mode frequencies are reported in Sec. IV A.

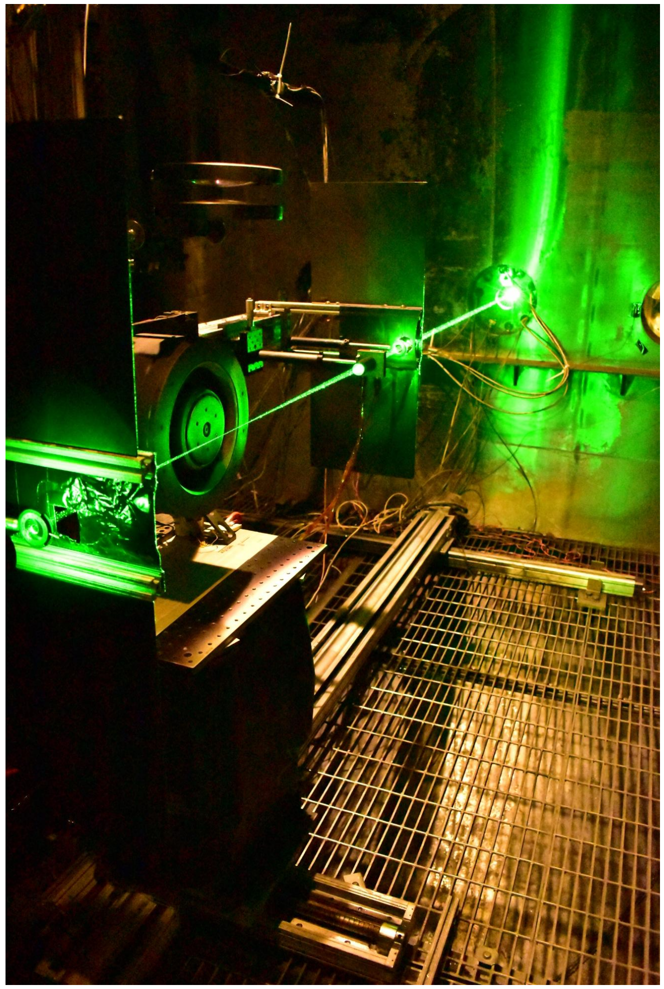

FIG. 1. Laser Thomson scattering system installed in the Georgia Tech VTF-2 vacuum chamber with the H9 Hall thruster, showing the laser beam path and spectrometer collection optics aligned for near-field measurements.

TABLE I. Operating conditions across the three configurations.

Parameter	Floating	Cathode-Tied	+2 V Bias
Body Voltage (V)	-1.54 ± 2.92	-10.4 ± 0.09	1.89 ± 0.29
Discharge Current (A)	40.2 ± 0.17	39.6 ± 0.11	39.4 ± 0.12
Discharge Voltage (V)	150 ± 0.16	150 ± 0.05	150 ± 0.08
Anode Flow (sccm-Kr)	402 ± 4.0	402 ± 4.0	402 ± 4.0
Cathode Flow (sccm-Kr)	28 ± 0.31	28 ± 0.31	28 ± 0.31
Bkgd. Pressure (μTorr-Kr)	7.73	7.73	7.73

B. Thruster Electrical Configurations and Circuit

Three distinct thruster body electrical configurations were examined. The electrical circuit for all three configurations is shown in Fig. 2, with corresponding instrumentation detailed in Table II.

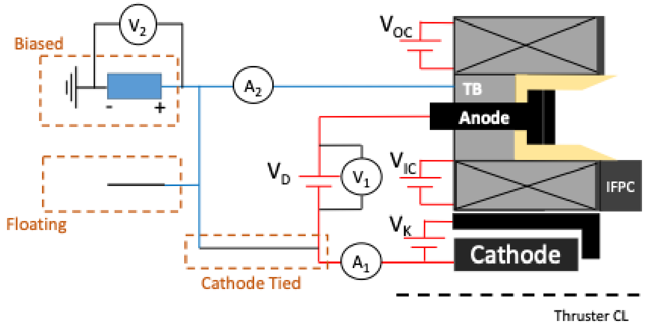

FIG. 2. Electrical circuit topologies for the three thruster body configurations: floating (isolated), cathode-tied (body connected to cathode), and +2 V bias (body held at +2 V relative to facility ground by an independent supply). Instrumentation labels correspond to Table II.

TABLE II. Electrical instrumentation corresponding to the circuit diagram in Fig. 2.

Parameter (Label)	Probe	Scope
Discharge current (A_1)	CP150	HDO6104
Discharge voltage (V_1)	DP-25	HDO6104
Body current (A_2)	CP150	HDO6104
Body voltage (V_2)	DP-25	HDO6104

Floating configuration: The thruster body is electrically isolated, with no connection to the cathode or to an external bias supply. The body potential settles to approximately −1.5 V relative to facility ground, and the body current is zero by definition since no external circuit exists.

Cathode-tied configuration: The thruster body is electrically connected to the cathode, placing the body at approximately −10.3 V relative to facility ground. The measured body current is +0.78 A. This is the flight-relevant configuration for magnetically shielded HETs.

+2 V bias configuration: The thruster body is biased to +2 V relative to facility ground using an independent DC power supply. The measured body current is −0.85 A.

A preliminary body current–voltage sweep was performed to identify a bias point that would produce a controlled electron current to the thruster body. Figure 3 shows the resulting characteristic, in which the body current reverses polarity near −2 V. The +2 V operating point was selected because its body current magnitude ($|I_{\text{body}}| \approx 0.85$ A) is comparable to the cathode-tied value ($|I_{\text{body}}| \approx 0.78$ A) but with opposite sign. This pairing isolates the effect of current direction on the near-field electron population while holding the current magnitude approximately constant.

C. Laser Thomson Scattering Measurement Locations

Measurement locations were distributed across the cathode near-field to characterize spatial variations in electron properties. A primary axial line was established along the cathode

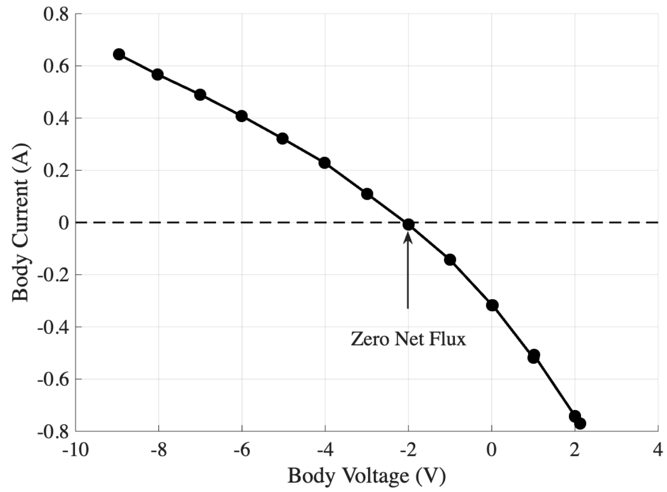

FIG. 3. Thruster body current as a function of body voltage from a preliminary bias sweep.

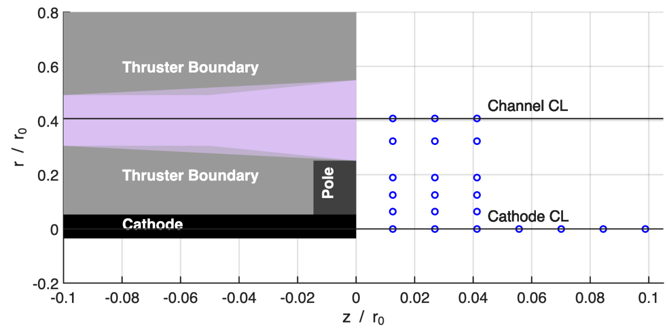

FIG. 4. Spatial map of laser Thomson scattering measurement locations in the r–z plane, showing the 22 probe points common to all three configurations (seven cathode-centerline axial stations and a 15-point radial grid). An eighth centerline station at $z/r_0 = 0.115$ was measured in the cathode-tied and +2 V configurations.

centerline ($r/r_0 = 0$) with measurements at eight axial stations from $z/r_0 = 0.014$ to $z/r_0 = 0.115$ (approximately 2 mm to 16 mm from the cathode orifice) for the cathode-tied and +2 V configurations, and at the first seven stations (to $z/r_0 = 0.101$) for the floating configuration. Additional radial profiles were obtained at selected axial distances. The spatial distribution of the 22 probe points common to the three configurations is shown in Fig. 4. Measurements were performed at a 45-degree azimuthal angle relative to the lab reference frame, an orientation selected to enable isolation of the radial electron bulk velocity through two orthogonal collection geometries (axial and azimuthal components of the scattered light).

The thruster geometry and coordinate system are defined in Fig. 5. Radial station designations L1 through L6 and their normalized radial positions relative to the cathode, IFPC (pole face), gap, and discharge channel are shown in Fig. 6; stations L1–L6 correspond to probe points P1–P6 in Fig. 5. A complete description of the experimental campaign, diagnostic implementation, and uncertainty analysis is available in Ref. 20.

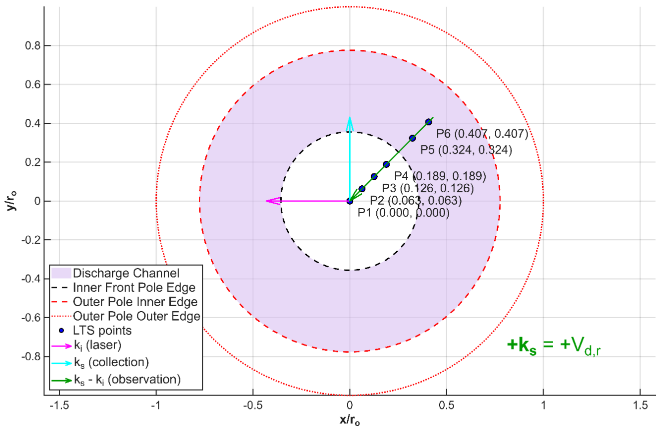

FIG. 5. H9 thruster geometry and coordinate system definition showing probe locations P1–P6 (corresponding to stations L1–L6) and scattering wave vectors. The cathode is located at $z = 0$, and the discharge channel centerline is at $r/r_0 = 0.4$.

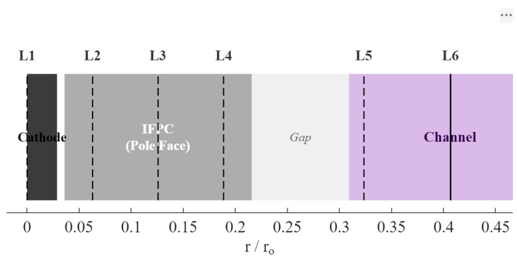

FIG. 6. Radial station designations L1 through L6 and their normalized radial positions relative to the cathode, IFPC (pole face), gap, and discharge channel. Stations L1–L6 correspond to probe points P1–P6 in Fig. 5.

IV. RESULTS

A. Discharge Stability and Power Spectral Density

All three electrical configurations operated stably throughout the experimental campaign. Figure 7 presents power spectral density (PSD) plots of the discharge current for each configuration. Breathing mode frequencies were measured at 6.24 kHz (floating), 6.37 kHz (cathode-tied), and 6.29 kHz (+2 V bias), all within 3% of each other and representing the dominant oscillation mode. These frequencies are approximately 57% lower than the 14.5 kHz breathing mode observed at the same 6 kW discharge power but lower discharge current (20 A, 300 V) by Butler-Craig *et al.*[21].

The less-than-3% variation in breathing frequency across configurations at 150 V, 40 A contrasts with the 18% shift observed between grounded and biased configurations at 300 V, 20 A by Butler-Craig *et al.*[21]. Su *et al.*[19] observed that the H9 discharge on krypton is more stable at higher current density, as reflected in lower breathing mode frequencies. The reduced sensitivity to body bias at 150 V, 40 A is consistent with this trend, as postulated by Butler-Craig *et al.*[21].

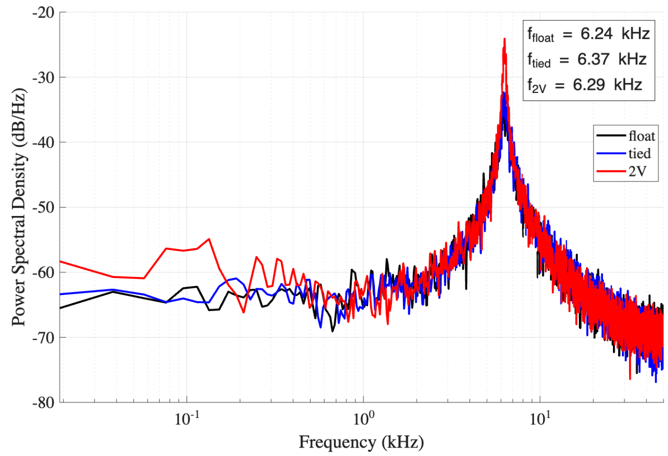

FIG. 7. Power spectral density of discharge current for the three electrical configurations.

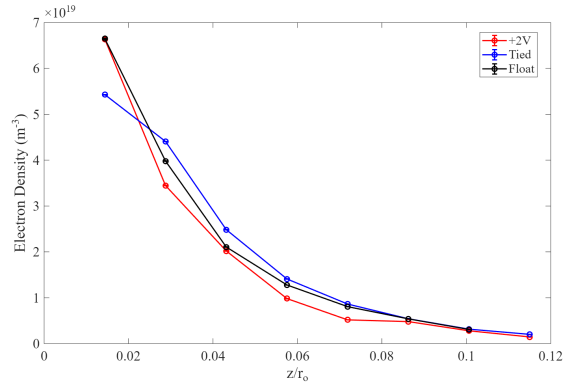

FIG. 8. Electron density along the cathode centerline ($r/r_0 = 0$) as a function of normalized axial position for the three electrical configurations.

B. Electron Density

Figure 8 shows electron density at the cathode centerline ($r/r_0 = 0$) as a function of axial distance. Beyond the first axial station, at $z/r_0 = 0.029$, the three configurations exhibit distinct density values: cathode-tied reaches 4.4×10^{19} m^{-3}, floating reaches 4.0×10^{19} m^{-3}, and +2 V reaches 3.4×10^{19} m^{-3}, a 26% spread across configurations. At the closest station ($z/r_0 = 0.014$), this ordering inverts: the cathode-tied configuration exhibits the lowest centerline density, while the floating and +2 V configurations are comparable. This near-orifice feature is examined in the Conclusions.

The electron density ranges from approximately 10^{19} m^{-3} near the cathode orifice to above 10^{17} m^{-3} at the outer radial positions. All three configurations follow the same spatial trend: density is highest near the cathode centerline and decreases by approximately two orders of magnitude with increasing radial distance.

Radial density profiles at fixed axial locations provide insight into radial transport (Figs. 9 and 10). A pronounced density depletion is observed at radial location L4 in the

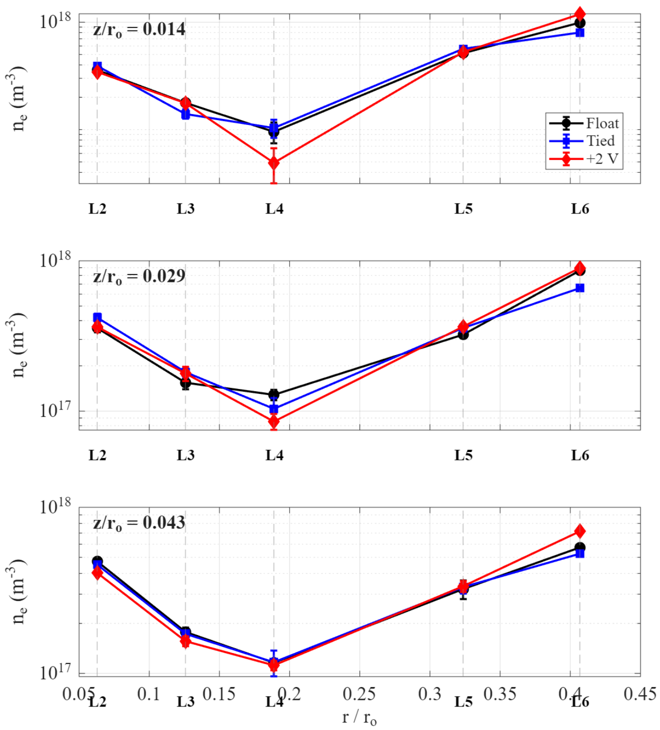

FIG. 9. Radial electron density profiles (logarithmic scale) as a function of radial position for three axial locations.

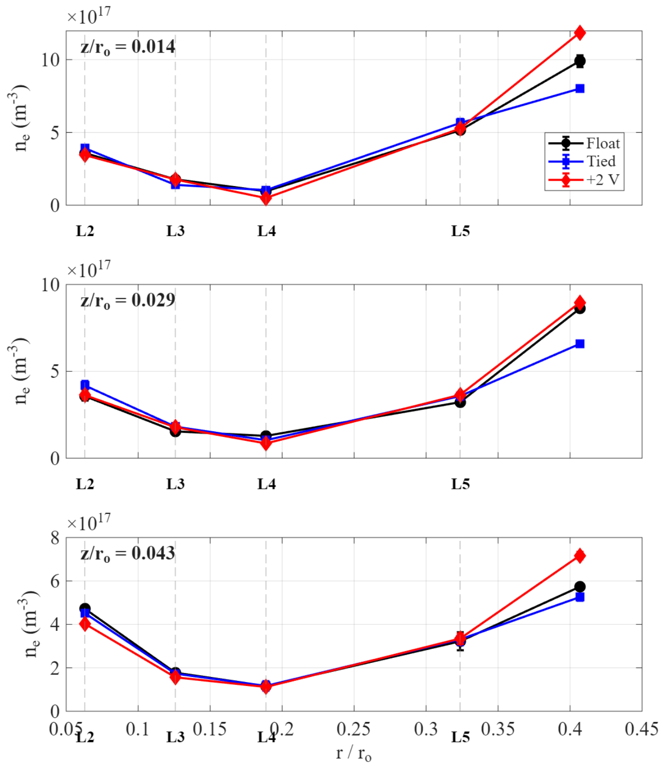

FIG. 10. Radial electron density profiles (linear scale) as a function of radial position for three axial locations.

+2 V configuration, where densities fall below 5×10^{16} m^{-3}. The floating-configuration cathode centerline peak density of 6.6×10^{19} m^{-3} is approximately 2.6 times the 2.5×10^{19} m^{-3} value reported by Suazo Betancourt *et al.*[7] at the 0-degree azimuthal angle under otherwise identical operating conditions.

At the axial station $z/r_0 = 0.014$ (approximately 2 mm from the exit plane), radial profiles reveal configuration-dependent differences. The +2 V configuration exhibits density values at radial location L4 that are factors of 2 to 3 below those of the floating and cathode-tied configurations. This depletion is spatially localized and does not extend to the channel centerline.

The data reveal a configuration-dependent spatial density inversion. The cathode-tied configuration maintains the highest electron density at the cathode centerline but the lowest density at the channel centerline (L6). The +2 V configuration shows the opposite: lowest density at the cathode centerline but highest at the channel centerline. This inversion indicates different electron circuit pathways for each body bias condition.

C. Electron Temperature

Electron temperature varies from approximately 3 to 5 eV in the near-cathode region to 25 to 32 eV at outer radial positions (Figs. 11 and 12). The cathode centerline temperatures are consistent with Suazo Betancourt *et al.*[7], who reported 2–3 eV near the cathode orifice increasing to 5–7 eV by $z/r_0 \approx 0.06$–0.08. Along the cathode centerline, the floating configuration is 0.35 to 0.4 eV (12 to 14%) higher than both cathode-tied and +2 V configurations near the cathode orifice.

D. Electron Pressure

Electron pressure is computed as $P_e = n_e k_B T_e$ from the measured density and temperature. Electron pressure exhibits a minimum in the IFPC region and increases toward the discharge channel. This qualitative pattern agrees with prior LTS measurements by Suazo Betancourt *et al.*[7]. A comparison with reference measurements at the same operating condition is shown in Fig. 13.

E. Radial Electron Bulk Velocity

Radial bulk velocity measurements are obtained from the Doppler shift of the Thomson scattering spectrum's center wavelength relative to the injection laser line λ_0. An electron population with a net directed velocity shifts the entire scattered Maxwellian profile by an amount proportional to the component of the bulk velocity along the scattering wave vector. By observing the Thomson spectrum from two orthogonal collection directions, the radial bulk velocity component can be isolated.

Two measurement constraints must be noted before inter-

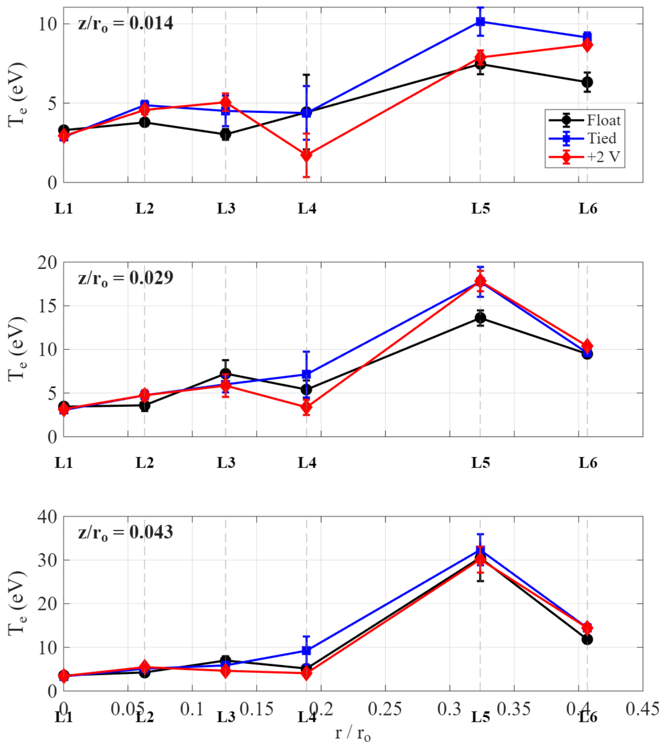

FIG. 11. Electron temperature as a function of radial position for three axial locations for the three electrical configurations.

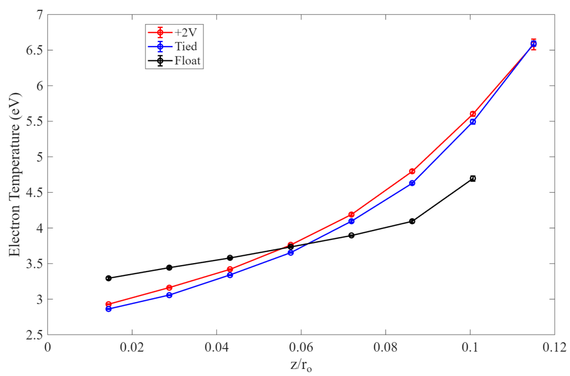

FIG. 12. Electron temperature along the cathode centerline ($r/r_0 = 0$) as a function of normalized axial position for the three electrical body configurations.

preting these results. First, the spectral resolution of the LTS system limits velocity sensitivity to approximately 18 km/s per detector pixel at 532 nm using the 1200 lines/mm grating, corresponding to a reciprocal linear dispersion of approximately 0.032 nm/pixel. Second, the absolute accuracy of the bulk velocity depends on the precision of the laser line wavelength calibration. Beyond these instrument-level constraints, an interpretive caveat also applies: the radial electron bulk velocity was measured to directly observe how body-bias conditions modify electron transport pathways in the near-field, and in principle a net radial bulk motion toward the thruster

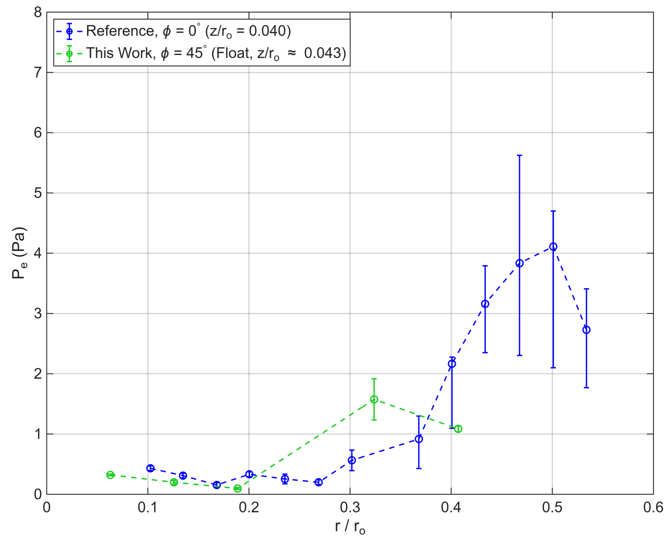

FIG. 13. Electron pressure as a function of radial position compared with reference measurements[7] at the same operating condition.

body in the cathode-tied configuration, or away from it in the +2 V configuration, would constitute direct evidence of configuration-dependent current pathways.

The cathode-tied and +2 V configurations exhibit the largest bulk velocity magnitudes at radial positions L3 to L4 near $z/r_0 = 0.015$ (approximately 2 mm), as seen in the spatial map of Fig. 14. Measured values reach 2.97×10^5 m/s (cathode-tied) and 1.97×10^5 m/s (+2 V). The floating configuration exhibits a different pattern, with the largest outward-directed bulk velocity at the cathode centerline.

Magnitudes up to 3.5×10^5 m/s (350 km/s) fall within the range reported by Vincent *et al.*[22], who measured the radial electron bulk velocity along the ISCT200 channel centerline from 2 to 40 mm downstream and observed values from −500 to +600 km/s depending on operating condition; the primary distinction is that the present measurements probe the cathode near-field rather than the channel downstream region. Along the cathode centerline (Fig. 15), the cathode-tied configuration maintains inward-directed (negative) radial velocities in the range from −37 to −20 km/s (toward the thruster axis), while the +2 V configuration maintains inward velocities from approximately −41 to −33 km/s through $z/r_0 = 0.05$.

Figure 16 presents the cathode centerline radial bulk velocity data as a vector arrow diagram, enabling simultaneous comparison of direction and relative magnitude across all three configurations and all axial stations. Arrow direction indicates the direction of radial bulk motion (leftward = radially inward toward the cathode centerline, negative V_d), and arrow length indicates relative magnitude.

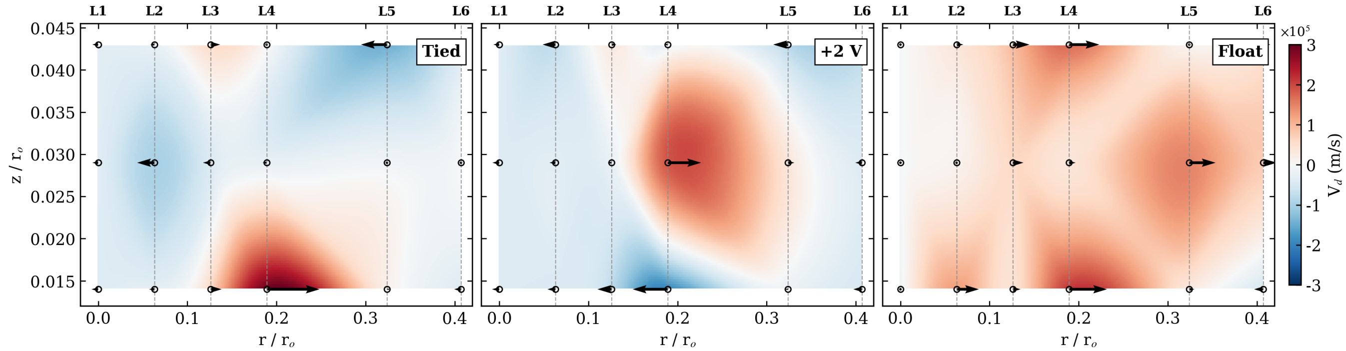

FIG. 14. Radial electron bulk velocity in the r–z measurement plane for the three electrical configurations. Color shows the V_d field interpolated between measurement locations (circles), and arrows show the measured vectors at each location. Positive V_d is directed radially outward toward the discharge channel; negative V_d is directed inward toward the cathode centerline. Values in the L1 column are taken from the cathode-centerline axial scan at matching axial positions.

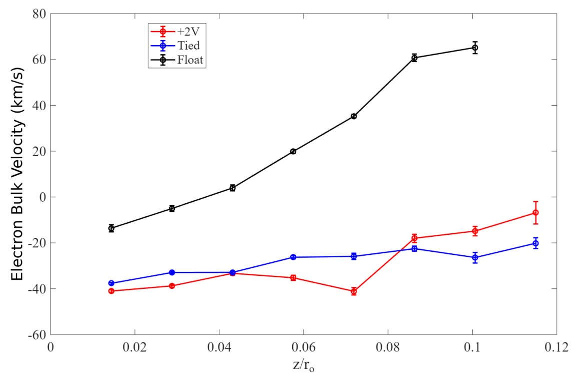

FIG. 15. Radial electron bulk velocity along the cathode centerline ($r/r_0 = 0$) as a function of axial position for the three thruster body electrical configurations.

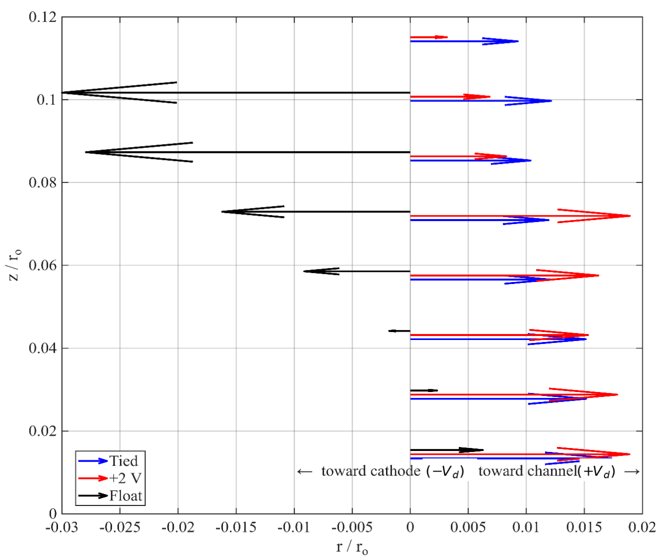

FIG. 16. Arrow diagram of radial electron bulk velocity vectors along the cathode centerline for the three electrical configurations.

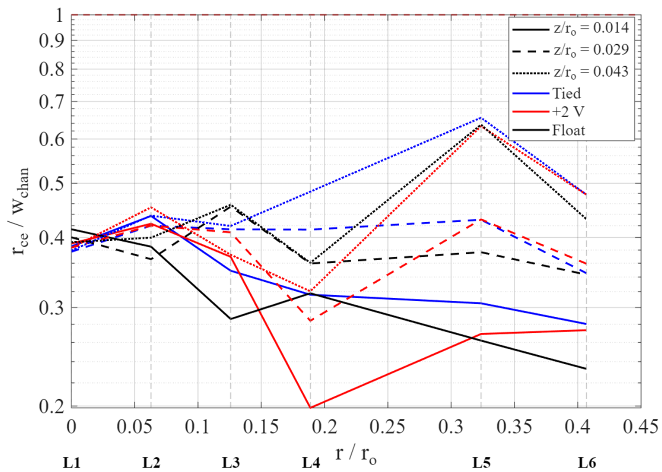

FIG. 17. Normalized gyroradius r_{ce}/r_o throughout the measurement domain.

V. DISCUSSION

A. Configuration-Dependent Electron Pathways

Before examining the circuit pathways, we note that electrons are strongly magnetized throughout the measurement domain: the normalized gyroradius satisfies $r_{ce}/r_o < 0.1$ everywhere, and the electron Hall parameter ranges from approximately 10–50 at the outermost stations to greater than 10^3 near the channel (Fig. 17). The millimeter-scale gyroradii in Fig. 17 reflect the low magnetic field magnitude in the near-field measurement domain, which lies downstream of the inner front pole where the field is well below its peak value near the channel exit, a defining feature of magnetically shielded topologies (field data for the H9 are export controlled and are specified only relative to the nominal setting, Sec. III A). Electron transport is therefore drift-dominated, and the spatial variations in density and temperature provide indicators of underlying current closure pathways.

The cathode centerline arrow diagram (Fig. 16) is consistent with this circuit-pathway picture, with the caveat that bulk velocities at the cathode centerline (L1) are near zero across all configurations and lie at or below the 18 km/s resolution floor, so the visual comparison at those stations should not be over-interpreted. The two patterns that survive the resolution analysis are: (1) the floating configuration reverses sign from inward to outward bulk motion at intermediate axial stations, and (2) the cathode-tied and $+2$ V configurations maintain unidirectional bulk motion throughout.

B. Spatial Density Inversion as Motivation for Pathway Analysis

All three configurations share a common baseline structure: density decreases by approximately two orders of magnitude from the cathode centerline to the outer radial positions, consistent with the expanding cathode plume. The spatial electron density inversion observed across the three configurations is superimposed on this baseline and is the empirical observation that motivates the pathway analysis below. Relative to the floating baseline, the cathode-tied configuration elevates electron density at the cathode centerline (beyond the first axial station, $z/r_0 \geq 0.029$) while depressing it at the channel centerline; the $+2$ V configuration produces the opposite pattern. This ordering is quantitatively consistent with the measured body current balance: the floating baseline carries zero net body current and produces intermediate centerline densities, the cathode-tied case draws $+0.78$ A of ion current to the body and produces the highest cathode-centerline density, and the $+2$ V case collects -0.85 A of electron current at the body and produces the lowest cathode-centerline density.

C. Configuration-Dependent Electron Pathways

In this work, an *electron pathway* refers to the path that cathode-emitted electrons must take to close the external electrical circuit set by the thruster body's boundary condition. Each of the three configurations imposes a different circuit closure requirement, and each leaves a measurable signature in the electron properties.

1. Floating Configuration (Baseline)

In the floating configuration, the thruster body has no external connection and the net body current is zero by construction (Fig. 18). The body potential settles to whatever value self-consistently balances ion and electron collection at its surface, here ~ -1.5 V relative to facility ground. Because no net current flows through the body, there is no circuit requirement for additional cathode-sourced electrons beyond those needed for the discharge. The electron density and temperature profiles in this configuration occupy the middle of the three cases at most stations and serve as the reference against which the two biased configurations are compared. The radial bulk velocity exhibits a different pattern from the biased cases: inward motion near the cathode transitioning to outward motion at larger axial distances.

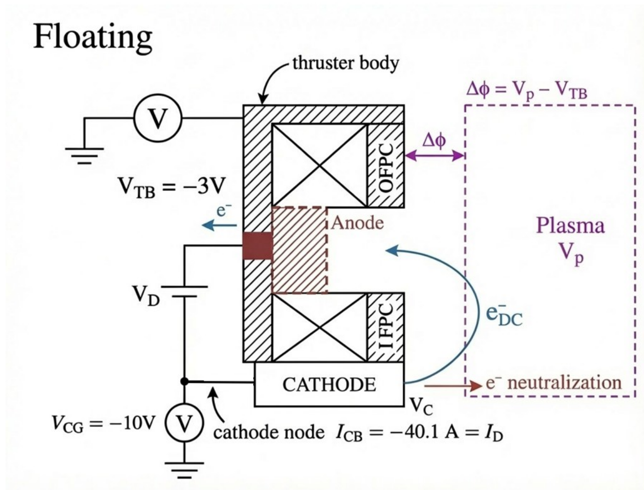

FIG. 18. Floating current pathway: the body has no external connection. Zero net body current occurs when ion and electron collection balance.

2. Cathode-Tied Configuration

In the cathode-tied configuration the body shares a common electrical node with the cathode (Fig. 19), placing it at approximately -10.3 V relative to facility ground. The measured body current is $+0.78$ A, indicating net ion collection at the body surface. The cathode must therefore emit additional electrons to close the body circuit[23,24]:

$$I_{\text{cathode}} = I_D + I_{T,\text{body}} \approx 40.4 \text{ A}, \tag{6}$$

where $I_D = 39.6$ A is the discharge current and $I_{T,\text{body}} = 0.78$ A is the body current. These additional cathode-sourced electrons must originate within the discharge; they are not transferred from facility ground.

The electron density signature is consistent with this picture. Relative to the floating baseline, the cathode-tied case raises the electron density at the cathode centerline (where the additional cathode-sourced electrons are injected) while depressing it at the channel centerline (where electrons are diverted toward the body).

3. $+2$ V Bias Configuration

In the $+2$ V bias configuration the body is held at $+2$ V relative to facility ground by an independent supply (Fig. 20). The measured body current is -0.85 A, indicating continuous electron collection at the body. These electrons cannot be replaced through any internal thruster circuit; in the ground-test

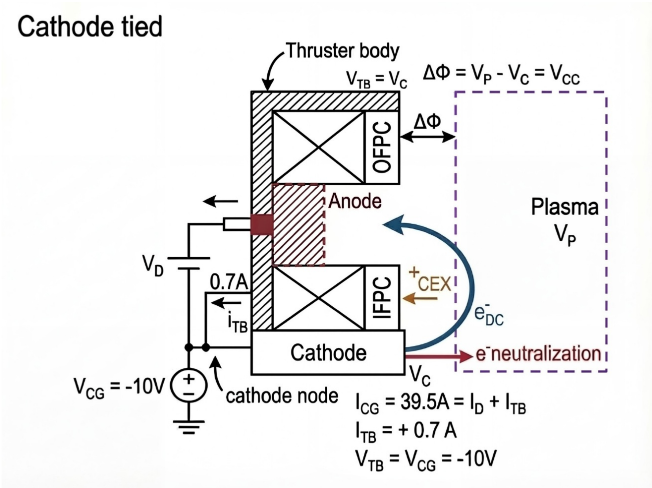

FIG. 19. Cathode-tied current pathway: the body node connects to the cathode through a wire, and ions collected at the body are neutralized by cathode-sourced electrons.

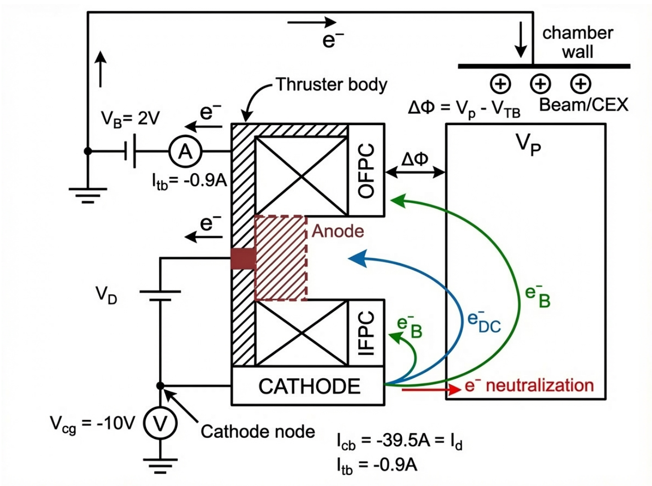

FIG. 20. +2 V bias current pathway: an independent supply holds the body at +2 V. Electrons from the plasma collect on the body; return current flows through facility ground paths.

environment, the return current flows through facility ground paths.

The electron density signature is the inverse of the cathode-tied case. Relative to the floating baseline, the +2 V case depresses the electron density at the cathode centerline and at intermediate radial positions where the body's collection field is strongest, with a pronounced local depletion at L4 on the IFPC surface. Meanwhile, the channel centerline density is elevated, consistent with electrons that are not diverted toward the body being pushed further into the channel.

The clearest +2 V effect is in the electron temperature at L4: 2–3 eV compared with 4.5–7 eV in the other two configurations. We attribute this reduction to magnetization-limited, energy-selective electron collection at the positively biased body. In an unmagnetized plasma, an attracting surface would collect electrons up to the electron saturation limit, with inertia as the only limiter, and no energy selectivity would be expected. Here, however, electrons are strongly magnetized throughout the measurement domain (Sec. V A): the normalized gyroradius satisfies $r_{ce}/r_o < 0.1$ and the Hall parameter exceeds 10 everywhere, so direct collection is impeded and electron flux to the IFPC requires cross-field transport. Because the cross-field displacement per scattering event scales with the gyroradius, and the gyroradius increases with electron energy, electrons in the upper portion of the energy distribution preferentially reach the body. The resulting depletion of the high-energy tail adjacent to the collecting surface reduces the effective temperature measured at L4.

D. Electron Pressure as a Proxy for Electrostatic Potential

A standard approximation in Hall thruster analysis assumes that electron pressure gradients determine the local electrostatic potential through the electron momentum equation. Under this assumption, the electric field is estimated as

$$E_r \approx \frac{1}{n_e q_e}\frac{dP_e}{dr}, \tag{7}$$

assuming the electron momentum equation reduces to a balance between pressure and electric forces. This reduction presumes a repelling boundary or otherwise impeded direct collection, and it further neglects anomalous transport terms that may become significant in strongly magnetized plasmas with instabilities.

Our measured electron pressure profiles (Fig. 13) show a minimum in the IFPC region and increase toward the discharge channel. If the simple pressure-gradient approximation were valid, this would indicate a radially inward electric field in the cathode near-field, driving ions away from the IFPC toward the discharge channel. However, the electron momentum equation in the presence of magnetic field, collisions, and plasma waves is

$$m_e n_e\left(\frac{\partial \boldsymbol{u}_e}{\partial t}+\boldsymbol{u}_e\cdot\nabla\boldsymbol{u}_e\right) = -n_e q_e \boldsymbol{E}+\boldsymbol{J}\times\boldsymbol{B} - \nabla P_e + \sum m_e \nu_{ei}(\boldsymbol{u}_e-\boldsymbol{u}_i)+\boldsymbol{F}_{\text{anom}}. \tag{8}$$

Two independent considerations preclude using Eq. (7) to infer the electrostatic potential in this region. First, in the +2 V configuration the boundary is attracting rather than repelling, so no balance of the Boltzmann form is established at the surface even in the absence of anomalous transport (Sec. V C 3). Second, for all three configurations the anomalous force term in Eq. (8), which includes contributions from plasma instabilities such as the modified two-stream instability (MTSI), electron cyclotron drift instability (ECDI)[25], and lower hybrid drift instability (LHDI)[26,27], is not constrained by our measurements and cannot be assumed negligible in the present domain ($\Omega_e \approx 10$–10^3). Therefore, electron pressure alone cannot serve as a reliable proxy for electrostatic potential in HET near-fields, and a complete determination would require measurement of the anomalous transport term or direct electric field measurements from alternative diagnostics (e.g., electric field probes or microwave scattering).

E. Limitations of the Radial Bulk Velocity Measurement

A fundamental limitation of radial bulk velocity measurements in this region must be acknowledged. As noted by Tsikata *et al.*[15] and Vincent *et al.*[22], the radial electron bulk velocity in the HET near-field is small relative to the azimuthal drift velocity driven by the $\boldsymbol{E} \times \boldsymbol{B}$ effect and diamagnetic pressure gradients. Because the radial component is a small projection of the total directed motion, measurement precision requirements are stringent, and systematic effects can dominate the uncertainty budget.

F. Practical Considerations for Configuration Selection

The three configurations present distinct advantages and disadvantages for practical HET operation. The *floating configuration* is operationally simplest, requiring no external connections or bias supplies. However, the floating potential is facility-dependent and varies with parasitic collection paths in the chamber, making results difficult to reproduce across different test facilities. The high variability in body voltage ($\pm$2.92 V) reflects this sensitivity.

The *cathode-tied configuration* is the flight-relevant design and provides electrical stability since the cathode voltage is well-defined by the discharge operating point. The body voltage relative to ground is predictable and reproducible.

The $+2$ *V bias configuration* provides excellent stability and the flattest discharge current across the experimental campaign, but the circuit pathways are not flight-relevant (electrons return to ground through facility walls). The energy-selective electron depletion at the IFPC is an artifact of the positively biased surface, not a phenomenon that would occur in space.

The $+2$ V configuration yields the lowest measured electron temperature at the IFPC (2 to 3 eV versus 4.5 to 7 eV in the other configurations), consistent with magnetization-limited, energy-selective electron collection at the positively biased surface. This signature is an artifact of the positive body bias and would not occur under the cathode-tied configuration used in flight.

Electron pressure gradients alone do not determine the local electrostatic potential in this region because anomalous transport contributions from plasma instabilities remain unconstrained. A complete determination of the electrostatic potential structure would require either direct electric field measurements or independent characterization of the anomalous force term.

A secondary observation warrants note. At the closest cathode-centerline station ($z/r_0 = 0.014$), the configuration ordering of electron density inverts relative to all downstream stations: the cathode-tied configuration exhibits the lowest centerline density, while the floating and $+2$ V configurations are comparable. A similar near-orifice inversion was observed in the electron property comparison of Butler-Craig *et al.*[21] at 300 V and 20 A, where it was treated as a statistical outlier because the measurements were not repeated. Its recurrence in the present campaign, at the same 6 kW discharge power but higher discharge current, suggests the feature is physical rather than anomalous. Identifying the responsible mechanism will require additional measurements; one candidate region is the immediate cathode orifice plume, where locally emitted electrons may dominate over the body-driven circuit pathways that govern the ordering downstream. This determination is left to future work.

VI. CONCLUSIONS

Spatially resolved laser Thomson scattering measurements in the near-field of the H9 magnetically shielded Hall effect thruster show that thruster body electrical bias produces measurable changes in electron density, temperature, and bulk velocity. A configuration-dependent spatial density inversion is observed: the cathode-tied configuration elevates density at the cathode centerline (4.4×10^{19} m^{-3} at $z/r_0 = 0.029$) while depressing it at the channel centerline, and the $+2$ V configuration produces the inverse pattern. This demonstrates that each electrical boundary condition imposes a different current closure topology. The ordering of densities across configurations is quantitatively consistent with the measured body currents.

These results establish a baseline mapping of how body bias redistributes electrons in the cathode near-field at a single operating condition. Extending the measurements to additional discharge voltages and currents would clarify the operational envelope of configuration-dependent effects. The elevated channel-centerline density in the $+2$ V configuration also raises the question of whether body-bias-driven electron pathway modification couples to ionization in the near-channel region, with possible implications for propellant utilization; investigating this coupling, and whether it persists outside the ground-test current closure paths, is left to future work. Quantitative determination of the anomalous transport terms remains a critical gap for predictive modeling of IFPC erosion in magnetically shielded Hall thrusters. The same cross-stream instabilities that leave the anomalous term unconstrained in this work are those invoked by Nikrant and Switzer[9] to explain the heating of the low-energy ion population responsible for the background-pressure-sensitive portion of IFPC erosion. A direct measurement of the anomalous transport term, or of the near-field electric field, would therefore serve both problems.

ACKNOWLEDGMENTS

N. I. Butler-Craig was supported by the NASA Space Technology Graduate Research Opportunities (NSTGRO) fellowship, Grant No. 80NSSC20K1224. The authors thank the High-Power Electric Propulsion Laboratory team at the Georgia Institute of Technology for experimental support, facility operations, and invaluable technical discussions.

AUTHOR DECLARATIONS

Conflict of Interest

The authors have no conflicts to disclose.

Author Contributions

Naia I. Butler-Craig: Conceptualization (lead); Investigation (lead); Formal analysis (lead); Methodology (lead); Visualization (lead); Writing – original draft (lead); Writing – review & editing (equal). **Julian Lopez-Uricoechea:** Investigation (supporting). **Richeek Dutta:** Investigation (supporting). **Mitchell L. R. Walker:** Supervision (lead); Funding acquisition (lead); Resources (lead); Writing – review & editing (equal).

Use of AI Tools

An AI-based language model (Claude, Anthropic) was used to assist with grammar editing and manuscript formatting during preparation of this article. The authors reviewed and take full responsibility for all content. No AI tools were used in the design, execution, or analysis of the research.

DATA AVAILABILITY STATEMENT

The data that support the findings of this study are available from the corresponding author upon reasonable request.

[1] D. M. Goebel and I. Katz, *Fundamentals of Electric Propulsion: Ion and Hall Thrusters* (Wiley, 2008).
[2] I. G. Mikellides *et al.*, Applied Physics Letters **102**, 023509 (2013).
[3] R. R. Hofer *et al.*, Journal of Applied Physics **115**, 043304 (2014).
[4] R. R. Hofer *et al.*, in *International Electric Propulsion Conference* (2017).
[5] B. A. Jorns *et al.*, in *AIAA Propulsion and Energy Conference* (2016).
[6] I. G. Mikellides *et al.*, in *AIAA Propulsion and Energy Conference* (2014).
[7] S. Suazo Betancourt *et al.*, Journal of Applied Physics **136**, 123301 (2024).
[8] T. Roberts *et al.*, Physics of Plasmas **31**, 083513 (2024).
[9] M. Nikrant and J. Switzer, in *AIAA SciTech 2024* (2024) p. 1140.
[10] T. Peterson *et al.*, in *AIAA Propulsion and Energy Conference* (2016).
[11] D. H. Froula *et al.*, *Plasma Scattering of Electromagnetic Radiation* (Elsevier, 2011).
[12] J. D. Jackson, *Classical Electrodynamics* (Wiley, 1998).
[13] M. Vincent *et al.*, Plasma Sources Science and Technology **27**, 055002 (2018).
[14] M. Vincent *et al.*, Plasma Sources Science and Technology **29**, 035015 (2020).
[15] S. Tsikata, B. Vincent, and S. Mazouffre, Physics of Plasmas **21**, 123506 (2014).
[16] S. Suazo Betancourt *et al.*, Journal of Applied Physics **135**, 083302 (2024).
[17] H. Kempkens and J. Uhlenbusch, Plasma Sources Science and Technology **9**, 492 (2000).
[18] D. W. Marquardt, SIAM Journal on Applied Mathematics **11**, 431 (1963).
[19] T. Su *et al.*, in *AIAA Propulsion and Energy 2020* (2020) p. 3617.
[20] N. I. Butler-Craig, *Experimental Investigation of Varied Thruster Body Bias on Electron Behavior in the Near-Field of a Magnetically-Shielded Hall Thruster*, Ph.D. thesis, Georgia Institute of Technology, Atlanta, GA (2026).
[21] N. Butler-Craig *et al.*, in *AIAA SciTech 2025* (2025) p. 1099.
[22] M. Vincent *et al.*, in *International Electric Propulsion Conference* (2019).
[23] D. M. Goebel *et al.*, Journal of Applied Physics **98**, 113302 (2005).
[24] I. G. Mikellides, I. Katz, D. M. Goebel, and J. E. Polk, Journal of Applied Physics **98**, 113303 (2005).
[25] S. Tsikata, C. Honoré, D. Grésillon, J. Cavalier, N. Lemoine, and G. Bonhomme, Physics of Plasmas **20**, 082107 (2013).
[26] T. Lafleur, S. D. Baalrud, and P. Chabert, Physics of Plasmas **23**, 053502 (2016).
[27] J. P. Boeuf, Journal of Applied Physics **121**, 011101 (2017).